JOM, Vol. 76, No. 6, 2024
https://doi.org/10.1007/s11837-024-06525-2

TECHNICAL ARTICLE

A New Method of Neodymium-Iron-Boron Magnets/Reduced Graphene Oxide Manufacturing Without a Controlled Atmosphere

J.C. SILVA FILHO ,[1,3] S.C. SILVA,[2] H. TAKIISHI,[2] S.R. JANASI,[2] L.G. MARTINEZ,[2] J.F.Q. REY,[1] and M.T. ESCOTE[1]

1.—Center of Engineer, Modelling and Applied Social Science, Federal University of ABC, Santo André, SP 09210-580, Brazil. 2.—Nuclear and Energy Research Institute, São Paulo, SP 05508-000, Brazil. 3.—e-mail: jorgecsilvaf@gmail.com

This paper introduces an innovative manufacturing method for NdFeB magnets, involving the integration of reduced graphene oxide (rGO) during mechanical milling (MM) to counteract powder ignition, a common issue in oxygen-rich environments. The NdFeB alloy underwent hydrogen decrepitation before being mechanically milled with varying rGO quantities in ambient air. Raman and X-ray diffraction (XRD) analyses confirmed the successful production of rGO samples with a minimal number of layers. The XRD analysis of the NdFeB/rGO powder demonstrated that all the diffraction peaks corresponded to the $Nd_2Fe_{14}BH_{1.86}$ phase, with no carbides or other carbon compounds detected. Transmission electron microscopy revealed rGO encapsulating the NdFeBrGO particles, while scanning electron microscopy of the resulting magnets (samples 1, 2, and 3) displayed grain sizes ranging from 0.5 μm to 6.8 μm. These manufacturing variations led to a diverse range of magnetic properties: remanence (Br) varied from 0.5 T to 1.13 T, intrinsic coercivity (iHc) ranged from 263.5 kA m^{-1} to 776.1 kA m^{-1}, and maximum energy product (BH_{max}) spanned from 21.0 kJ m^{-3} to 232.3 kJ m^{-3}. Remarkably, the most favorable Br, iHc, and BH_{max} values were observed in Sample 0.02 wt.% rGO, closely aligning with the characteristics typically found in commercial NdFeB.

INTRODUCTION

Neodymium–iron–boron (NdFeB) magnets are commonly referred to as the third generation of rare-earth permanent magnets, distinguished by their exceptional balance of coercivity, remanence, and maximum energy product.[1] However, the magnetic properties of NdFeB magnets are often influenced by the quality of the NdFeB-based powders and the manufacturing processes, resulting in variations in microstructure and magnetic behavior.[1] Given their high susceptibility to oxygen reactivity, it is necessary for strict atmospheric control to produce fine NdFeB-based powders, typically achieved using a glovebox or inert gases. Exposure to oxygen during the grinding process can lead to autoignition, causing surface oxidation, phase segregation, and the deterioration of desired magnetic properties in the final product.[2] In the literature, methods for enhancing oxidation resistance are primarily discussed in the context of sintered magnets rather than powdered materials. For sintered magnets, organic coatings are often applied, utilizing various precursors to improve the protective properties of the surface coating, depending on the specific organic material employed.[3] In this context, Lopes et al.,[4] and Sasaki et al.,[5] detailed the incorporation of carbon with a binder/additive in the fabrication process of NdFeB magnets. Additionally, Xia et al.,[6] recently examined the impact of carbon and oxygen on the magnetic properties of

(Received May 25, 2023; accepted March 13, 2024; published online April 10, 2024)

NdFeB magnets. Carbon impurities have been shown to influence the coercive force in both sintered and optimally heat-treated samples.[6] The interaction between carbon and NdFeB introduces complex defects likely to reduce intrinsic coercivity.[4,6] Investigations have shown that the phase responsible for the hard magnetic properties is $Nd_2Fe_{14}B$, which has an easy magnetic direction along the *c*-axis.[7] Furthermore, the microstructure includes grains of the $NdFe_4B_4$ phase, forming grain boundaries within the Nd-rich matrix phase.[8]

This paper presents a novel methodology for producing NdFeB permanent magnets using powder metallurgy. Firstly, we synthesized and characterized reduced graphene oxide, subsequently used to prepare the NdFeB-rGO composite via mechanical milling (MM) without requiring strict atmospheric control. In this process, rGO is a protective agent, preventing oxidation and ignition. Secondly, this work investigates the impact of rGO additions (0.02–0.10 wt.%) on the milling process and its influence on the magnet's properties. Finally, the paper provides an overview of the structural and magnetic properties of the resulting sintered magnets.

EXPERIMENTAL

Materials and Preparation of Composite Powders

A commercial strip casting alloy with the nominal composition $Nd_{30.21}Pr_{0.64}Fe_{63.64}B_{0.94}Co_{2.93}Dy_{1.05}Cu_{0.15}Al_{0.15}Ga_{0.21}$ (wt.%) (referred to as NdFeB), weighing 15 g, underwent hydrogen decrepitation (HD) at a room temperature of 100 kPa pressure, transforming into a brittle material in the form of a metallic hydride.

Reduced graphene oxide (rGO), prepared following the literature,[9] was added with concentrations of 0.1, 0.03, or 0.02 wt.% to the decrepitated alloy, then the samples were homogenized and grounded during the MM, which was performed in an air atmosphere using a high-energy planetary mill (Premium line Pulverisette 7; Fritsch) at a speed of 200 rpm for 45 min[10] and a ball-to-powder ratio of 10:1. Without atmospheric control, these powders were then carefully placed into a polymeric template and subjected to a pulsed magnetic field of 6 T to align the grains. Subsequently, the powders were isostatically pressed at 200 MPa. The sintering process for the compacted powders involved three sequential steps: (1) initial heating at 593 K (10 K per min); (2) second-stage heating at 973 K (10 K per min); and (3) a final heating step, reaching a maximum temperature of 1333 K (7 K per min) for 1 h, following a procedure previously outlined elsewhere.[11]

Characterization

All the samples produced, including the rGO powder, the NdFeB/rGO composite, and the final magnets, were characterized by X-ray diffraction (XRD; D8 Focus; Bruker)using a Cu-Kα radiation source, with 40 kV and 30 mA. Using PowderX software, we estimate the structural parameters such as lattice parameters, full width at half maximum of the peaks, and interplanar spacing.[12] The crystallite size was calculated using Scherrer's expression:[13]

$$\left(D = \left(\frac{k\lambda}{\beta \cos\theta}\right)\right) \tag{1}$$

where β represents the full width at half maximum of the diffraction peak, and K (0.9 Å) is the shape factor.[14]

To accurately assess peak broadening in the X-ray patterns of our samples, we utilized the highly effective Williamson–Hall (W-H) methodology. This approach enabled us to establish a clear relationship between the width of the peaks and both crystallite size and lattice strain. By constructing the W-H plot], we obtained precise and reliable results:[15]

$$\beta_{hkl} \cos\theta = \left(\frac{k\lambda}{D}\right) + (4\varepsilon \sin\theta) \tag{2}$$

where β_{hkl} signifies the full width at half maximum of the X-ray peaks, k represents the shape factor (0.9), D is the crystallite size, λ is the wavelength of Cu-Kα radiation, and ε is the lattice strain. $\beta_{hkl} \cos\theta$ versus $\sin\theta$ plots were used to estimate the D and ε values for each sample.

Raman spectra were recorded in the range of 500–2000 cm^{-1} using a Raman WITEC Alpha 300r-green laser microscope; 532 nm; 45 mW.

For magnetic characterization of the sintered samples, an LDJ model BH-5000 Permeameter was employed. Remanence (Br) and intrinsic coercivity (iHc) values were extracted from the second quadrant of the hysteresis cycle (demagnetization curve). A scanning electron microscope (SEM; JSM-6610LA; JEOL) operating at an acceleration voltage of 20 keV was utilized for microstructural analysis. The density of the magnets was determined using the Archimedes principle.[16]

RESULTS AND DISCUSSION

First, we conducted structural characterization of the rGO employed in the milling process for the NdFeB samples using XRD and Raman spectroscopy to assess its properties. Figure 1a displays the XRD pattern of the rGO sample, revealing two distinctive peaks at $2\theta \approx 25°$ and 43°, corresponding to the (002) and (102) planes of rGO, respectively.[17] The broad peak observed at $2\theta \approx 25°$ suggests the presence of a few layers of rGO sheets within this

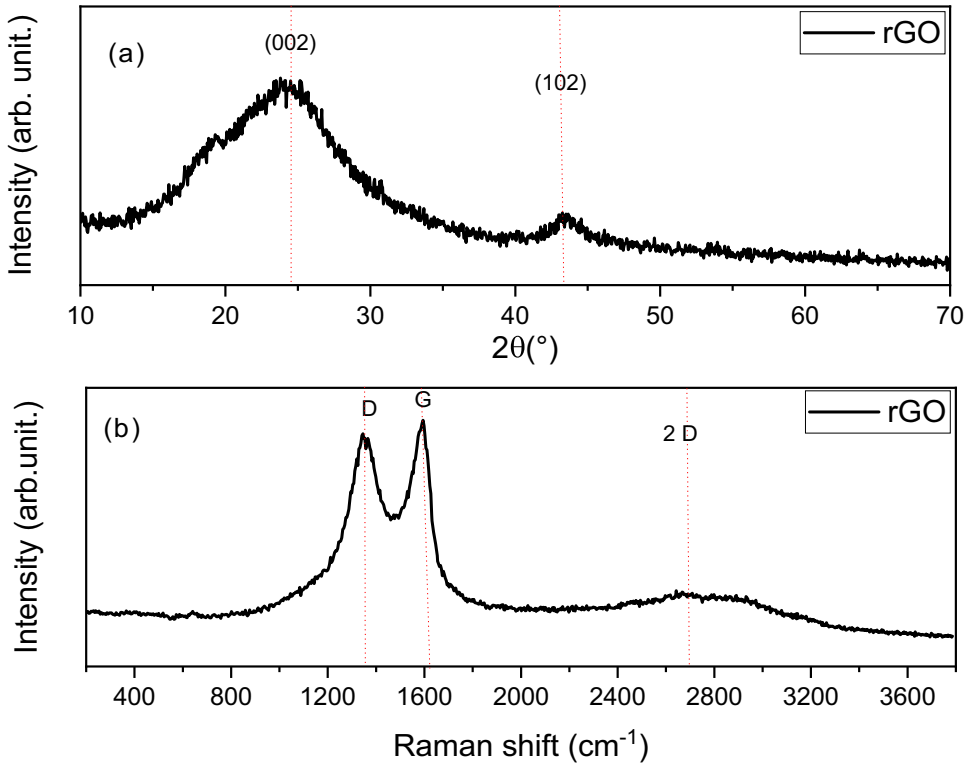

Fig 1. (a) XRD pattern and (b) Raman spectrum of the rGO powder.

sample. Furthermore, the shoulder around 16° may indicate the potential intercalation of oxygen groups or water molecules between the rGO layers.[17] Using Eqs. 1 and 2, we calculated vital parameters such as crystallite size, the number of layers, and interplanar distance, yielding values of 3.8 Å, 9.2 nm, and 3 layers, respectively.

The Raman spectrum of the rGO is depicted in Fig. 1b, which exhibits three discernible bands: *D*, *G*, and 2D at 1347.59 cm^{-1}, 1593.05 cm^{-1}, and 2725.13 cm^{-1}, respectively. The first peak is associated with defects related to sp^3 carbon bonds (*D* band), the second peak is indicative of sp^2 carbon atoms (G band), and the third peak is attributed to defects in the graphene structure (2D band).[18]

The sheet-like morphologies of the rGO samples are further evident in Fig. 2a and b, showcasing the presence of rGO sheets enveloping NdFeB particles following the milling process. The microstructure reveals distinct regions with varying contrasts, where the NdFeB-based powder phase exhibits a darker atomic contrast, while the rGO occupies lighter regions, encompassing the NdFeB particles.

Figure 3a shows the XRD patterns of HD NdFeB powders ground with different amounts of rGO, precisely 0.02, 0.03, and 0.1 wt.%. All the observed diffraction peaks can be attributed to the $Nd_2Fe_{14}BH_{1.86}$ (ICSD 80973) phase, with no discernible peaks indicating the presence of carbides or other carbon compounds. These findings suggest that the structural integrity remains unaltered in response to the introduction of graphene during the milling process. These powders were subsequently employed in the fabrication of magnets, denoted as magnet1 (0.1 wt.% of rGO), magnet2 (0.03 wt.% of rGO), and magnet3 (0.002 wt.% of rGO), with their respective X-ray patterns presented in Fig. 2b.

As depicted in Fig. 3b, all the Bragg reflections correspond to the crystalline NdFeB phase, characterized by a tetragonal structure with space group symmetry *P*42/*mnm*, as documented in the ICSD 29747 file. Upon comparing Fig. 3a and b, a marked distinction in the X-ray diffraction peaks is evident, attributed to the random and texturized orientation of the crystallites, respectively. The observed texturization in these X-ray patterns results from the arrangement of the magnets and is exemplified by the preferential reflections (002) and (105) (see Fig. 3b). Similar findings have been reported in the literature.[19] Moreover, a detailed examination of these X-ray diffractograms for Magnet1 and Magnet2 unveiled two low-intensity peaks at approximately $2\theta \sim 30.70°$ and 44.40°, with both peaks indicating the presence of a minor quantity of Nd_2O_3 and Fe-α, respectively.[20,21]

The structural parameters of the NdFeB magnet phases are provided in Table I, which presents the calculated values of lattice parameters *a*, *b*, *c*, and the unit cell volume V. These values exhibit a decreasing trend with the increasing rGO content utilized during the grinding process. This phenomenon is believed to be a consequence of the surplus carbon introduced during heat treatment, resulting in the alteration of these structural

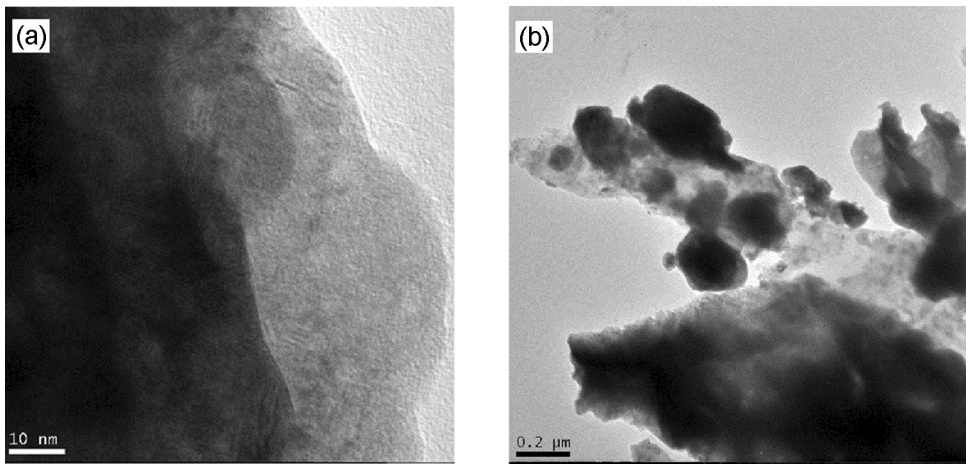

Fig 2. (a) Transmission electron microscope images showing the contrast of NdFeB-based powders atoms at the edges of rGO, and (b) NdFeB-based powder cover of rGO.

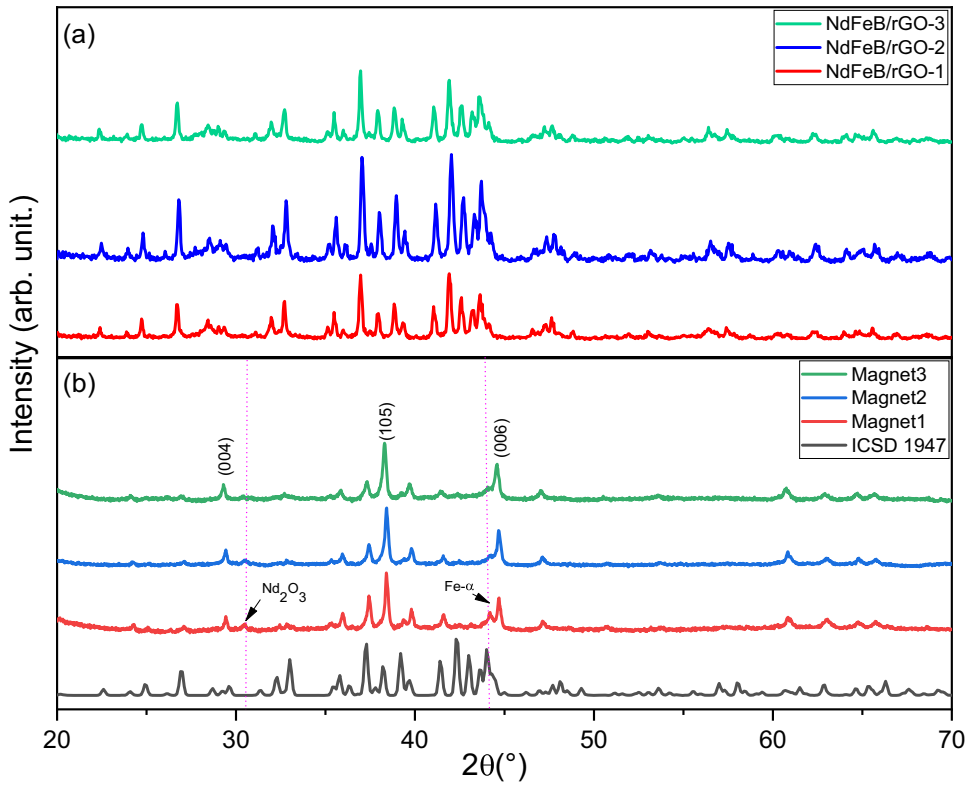

Fig 3. (a) X-ray diffraction patterns of HD powders produced with different amounts of rGO additions on commercial NdFeB alloy; (b) X-ray diffraction of the magnets: Magnet1, 0.1 wt.% of rGO (red line), Magnet2, 0.03 wt.% of rGO (blue line), and Magnet3, 0.002 wt.% of rGO (black line) (Color figure online).

Table I. Lattice parameters of the phases of the magnets

Sample	*a* (Å)	*b* (Å)	*c* (Å)	*V* (Å)
ICSD29747	8.8088 (5)	8.8088 (5)	12.2157 (1)	946.18
Magnet1	8.8203 (3)	8.8203 (3)	12.2316 (4)	951.60
Magnet2	8.8097 (2)	8.8809 (3)	12.2265 (3)	948.01
Magnet3	8.8030 (6)	8.8030 (6)	12.2198 (8)	946.94

parameters and encouraging the segregation of Nd_2O_3 and Fe-α. Since the neodymium-rich phase is a non-ferromagnetic phase, it is anticipated to impact the magnetic properties of the sintered NdFeB magnet.[22] Therefore, the distribution of the Nd-rich phase plays a crucial role in the magnetization and demagnetization processes of the sintered NdFeB magnet.

Table II. *D* values estimated through the lattice stress, and Scherrer and Williamson–Hall plots

Sample	D_s (nm)	$D_{W\text{-}H}$ (nm)	ε
Magnet1	39.1	36.4	-2.0×10^{-4}
Magnet2	41.5	35.6	-3.4×10^{-4}
Magnet3	45,3	38.7	-3.35×10^{-5}

Table II provides the D values estimated using both the Scherrer and W-H plot methods (see Figure S1 in the Supplementary file), as well as the lattice stress. The D values obtained using both methods closely align with those reported in the literature for the NdFeB samples. Notably, both the D_s and $D_{W\text{-}H}$ values decrease with the augmentation of graphene content employed during the milling process. The negative ε values observed are attributed to the defects introduced during the processing of these alloys.[23]

Figure 4a, c, and e illustrates the microstructures of sintered magnets manufactured with different rGO contents. These microstructures reveal the presence of small voids within the 2:14:1 matrix phase, as indicated by the red arrows in the micrographs, likely attributed to the introduction of rGO. Incorporating larger quantities of rGO leads to an increase in the number of voids within the magnet microstructure, which facilitates the demagnetization process of the magnets, as observed in Fig. 3 (Magnet2 and Magnet3).

During the thermal reduction process of graphene oxide to obtain rGO, it has been reported that explosions can occur due to rapid heating.[24] Given the high-speed initial heating rate employed during the sintering of the magnets (10 K per min) up to 593 K, it is plausible that such a phenomenon could have occurred in the magnets. The release of hydrogen from the HD powder towards the conclusion of the initial sintering stage at 593 K may have interacted with the smaller content of oxygen liberated by the rGO, resulting in the formation of the small voids observed in the micrographs of Fig. 4b, c, and d. The quantity of these small voids influences the densities of the sintered magnets. Magnet1, with a higher void content, exhibited a lower density of 6890 kg m^{-3} compared to Magnet3, which possessed a density of 7250 kg m^{-3}. Enhancement of the properties of the sintered magnets achieved through the addition of rGO as a milling agent can be realized by reducing the heating rate during sintering or by employing rGO with reduced quantities of hydroxyl groups, as suggested in the literature.[9]

Figure 5 illustrates the demagnetization curves for magnets 1, 2, and 3. The increase in rGO content during the MM process results in a reduction in the magnetic properties of the resulting magnets, leading to decreased values of remanence (Br) and maximum energy product ($(BH)_{max}$), as detailed in Table III. Remanence (Br) ranged from 0.5 T (0.1 wt.% rGO) to 1.13 T (0.02 wt.% rGO), intrinsic coercivity (iHc) varied from 263.5 kA m^{-1} (0.1 wt.% rGO) to 776.1 kA m^{-1} (0.02 wt.% rGO), and the energy product fluctuated from 21.0 (kJ m^{-3}) to 232.3 (kJ m^{-3}), as shown in Fig. 5b. These differences in coercivity properties can be attributed to the presence of voids within the magnets, induced by the carbon and oxygen in the NdFeBrGO-based powders, as well as the segregation of the Nd_2O_3 phase in Magnet1 (Fig. 4a). The Nd-rich phase at the grain boundaries reacts with impurities during the sintering process. The increase in coercivity observed in Magnet3 is more pronounced with 0.02 wt.% rGO during milling, compared to the higher content of 0.1 wt.% rGO in Magnet1. These results underscore the significant impact of carbon impurities on the processing, primarily due to the formation of Nd_2O_3. The reduction in the quantity of the Nd-rich phase exerts an influence on the magnetic properties because it is responsible for pinning the domain walls.[3] As the Nd-rich grain boundaries deteriorate, the effective coercivity (Hc) decreases rapidly, as evidenced in the demagnetization curves presented in Fig. 5a. Similar outcomes were reported by Fim (2018), who achieved Br = 1.02 T, iHc 652.5 kA m^{-1}, and BH_{max} = 143 kJ m^{-3} with a different processing approach that did not involve the addition of GO.[25]

In this context, it is evident that remanence and coercivity decrease as the particle size distribution decreases, as depicted in Fig. 4b, d, and f. Magnet1 and Magnet2 exhibited grain sizes below 1 μm, resulting in lower coercivity, owing to the established dependence of coercivity (Hc) on grain size, which is significant for sizes exceeding 3 μm. Additionally, the X-ray results of these two magnets also suggested the presence of a segregated neodymium phase, which can contribute to their poor magnetic properties.[26] In fact, previous research reported by Sasaki (2015) has indicated that the detrimental effects of impurities are more prominent in samples with grain sizes below 3 μm.[5] The further reduction in the quantity of the Nd-rich phase may be attributed to the quantity of reduced graphene oxide added during the MM.[27] Moreover, Magnet3 presents the largest grain size, measuring 6.8 μm compared to the other samples, also contributing to superior magnetic properties. This observation aligns well with the measurements of magnet density, and detailed magnetic property valuesprovided in Table III.

CONCLUSION

The XRD results confirmed the presence of the $Nd_2Fe_{14}BH_{1.86}$ phase, with no discernible peaks of carbon or carbides detected in the three different samples of NdFeB powders processed with varying rGO contents. However, after pellet pressing and heat treatment, the crystallographic structure was retained, but a small amount of additional Nd_2O_3 phase was observed in Magnet1 and Magnet2. This phase segregation also influenced lattice parameters, crystallite size, and grain size. In fact, with a

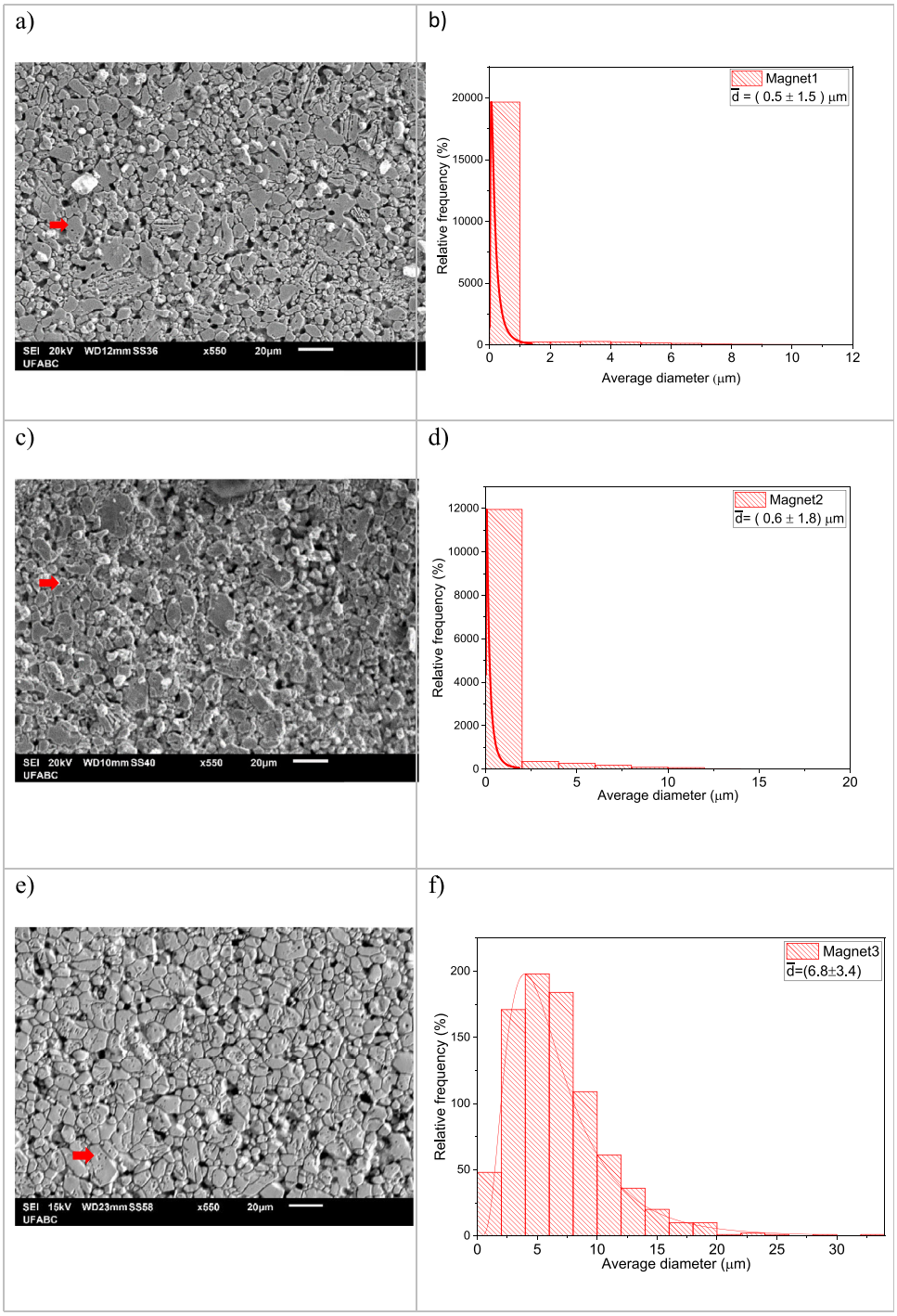

Fig 4. (a) SEM images, (b) mean grain size of Magnet1, and (c) SEM images and (d) mean grain size of Magnet2, (e) SEM images, and (f) mean grain size of Magnet3.

decreasing amount of rGO, the average particle size reached 6.8 μm, while the grain size of the corresponding sintered magnets (Magnet1 and Magnet2) decreased to less than 1 μm. Given that the coercivity and remanence of sintered NdFeB magnets are strongly dependent on the grain size, we observed that Magnet3, with 0.02 wt.% of rGO, exhibited superior magnetic properties in comparison to Magnet1 with 0.1 wt.% rGO. The remanence (Br) and intrinsic coercivity (iHc) of these magnets increased from 0.5 T to 1.13 T and from 263.5 kA m^{-1} (0.1 wt.% rGO) to 776.1 kA m^{-1}, respectively.

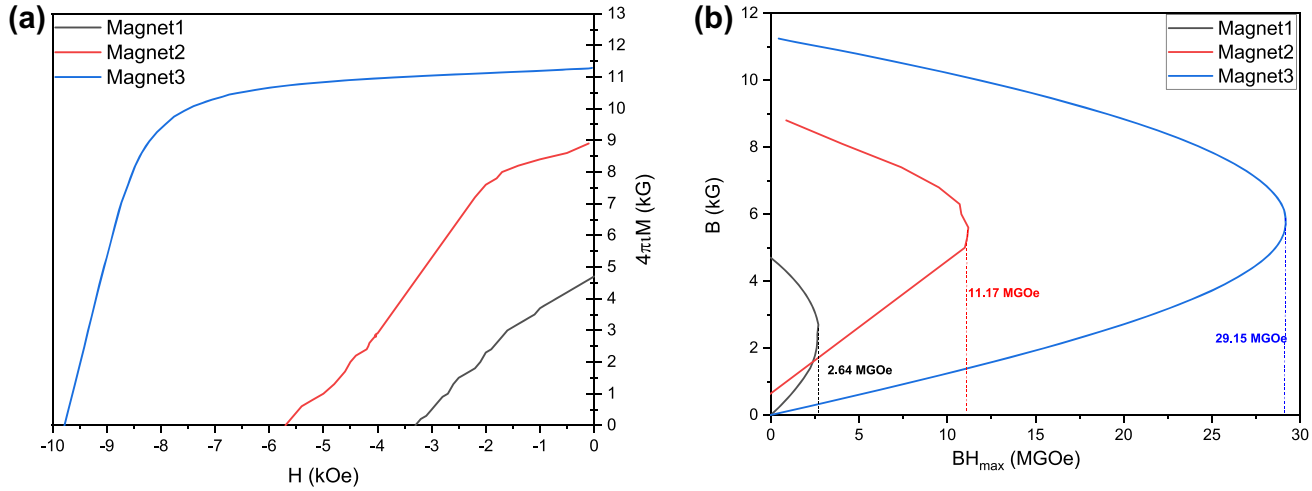

Fig 5. (a) Demagnetization curves of the magnet produced with the addition (0.02, 0.03 to 0.10 wt.%) of different contents of rGO as milling agent, and (b) energy products of the magnets.

Table III. Percentage of rGO, magnetic properties, and density of the magnets produced

Sample	rGO (wt.%)	iHc (kOe)	Br (kg)	BH_{max} (MGOe)	ρ (kg m^{-3})	Relative density (%)
Magnet1	0.10	3.31	4.86	2.64	6890	91
Magnet2	0.03	5.67	8.90	11.17	6974	92
Magnet3	0.02	9.75	12.29	29.15	7250	96

SUPPLEMENTARY INFORMATION

The online version contains supplementary material available at https://doi.org/10.1007/s11837-024-06525-2.

ACKNOWLEDGEMENT

National Council for Scientific and Technological Development (CNPQ) project: 400872/2019-6 and 142164/2020-8 process. CNPQ project: 440742/2020-0. The National Institutes of Science, Technology and Innovation Program (INCT Project): CNPQ (465719 / 2014-7), São Paulo Research Foundation (FAPESP -2014/50887-4) and Coordination of Superior Level Staff Improvement (CAPES - 23038000776/2017-54), the Materials Science and Technology Center (CECTM/IPEN), Laboratory of Electrical Engineering (POLI/USP), the National Graphite and IPEN-CNEN/SP. Laboratory of Functional Polymers, Laboratory of Surface Engineering from Federal University of ABC (UFABC) and the Multiuser Laboratory Facility (CEM-UFABC).

AUTHOR CONTRIBUTIONS

Silva-Filho: Conceptualization, Writing—Original Draft, Writing, Review & Editing, Funding acquisition. Silva: Investigation, writing, formal analysis. Takiishi: Conceptualization, Investigation, Formal analysis. Janasi: Investigation, Formal analysis. Martinez: Investigation, Formal analysis. Rey: Investigation, Formal analysis. Escote: Conceptualization, Writing Review & Editing.

DATA AND CODE AVAILABILITY

Data will be made available on request by e-mail.

CONFLICT OF INTEREST

The authors declare that they have no known competing financial interests or personal relationships that could have appeared to influence the work reported in this paper.

REFERENCES

1. Y. Liu, J. He, H. Yu, X. Zhong, Y. Liu, X. Li, and Z. Liu, *J. Magn. Magn. Mater.* 516, 167339 https://doi.org/10.1016/j.jmmm.2020.167339 (2020).
2. H. Takiishi, L.F.C.P. Lima, I. Costa and R.N. Faria. *PT* 127, 223. https://doi.org/10.1016/S0032-5910(02)00152-3 (2002).
3. P.K. Sokolowski, Processing and protection of rare earth permanent magnet particulates for bonded magnet applications (Iowa State University, 2007). https://doi.org/10.31274/rtd-180813-16220.
4. L.U. Lopes, E.C. Santos, T. Hartwig, and P.A. Wendhausen, *IEEE*. https://doi.org/10.1109/INTMAG.2015.7156603 (2015).
5. T.T. Sasaki, T. Ohkubo, Y. Une, H. Kubo, M. Sagawa and K. Hono. *Acta Mater.*, 84, 506. https://doi.org/10.1016/j.actamat.2014.10.047 (2015).
6. M. Xia, A.B. Abrahamsen, C.R.H. Bahl, B. Beluri, A. Søegaard, P. Bøjsøe, and S. Millot, *J. Magn. Magn. Mater.* 422, 232 https://doi.org/10.1016/j.jmmm.2016.09.014 (2017).

7. M. Sagawa, S. Fujimura, N. Togawa, H. Yamamoto, and Y. Matsuura, *J. Appl. Phys.* 55(6), 2083 https://doi.org/10.1063/1.333572 (1984).
8. Y. Li, X. Xu, M. Yue, T. Ma, and W. Liu, *J. Magn. Magn. Mater.* 508, 166847 https://doi.org/10.1016/j.jmmm.2020.166847 (2020).
9. J.C. Silva-Filho, E.C. Venancio, S.C. Silva, H. Takiishi, L.G. Martinez, and R.A. Antunes, *SN Appl. Sci.* 2(8), 1 https://doi.org/10.1007/s42452-020-03241-9 (2020).
10. J.C. Silva-Filho, S.C. Silva, R.G.T. Fim, H. Takiishi, Preparation of magnetic, ferrous, and non-ferrous powders, using rGO, GO and G as milling agents. *Brazilian National Institute of Industrial Property*, (BR. Patent no10 2019 016267 8).
11. M.R. Da Silva, R.G.T. Fim, S.C. Silva, J.C.S. Casini, P.A. Wendhausen and H Takiishi H., *Mater. Sci. Forum* 930, 440. https://doi.org/10.4028/www.scientific.net/MSF.930.440 (2018).
12. C. Dong, *J. Appl. Crystallogr.* 32, 838 (1999).
13. R.W. James, X-Ray Crystallography. *John Wiley and Sons Inc* (1961).
14. B.D. Culitt, Elements of X-Ray Diffraction, *Addlson-Wesley Publishing Company*, Inc. (1956).
15. W. Liu, M. Zhang, K. Zhang K and Y. Chai Y., *Adv. Condens. Matter Phys*. https://doi.org/10.1155/2017/4296243 (2017).
16. P. Sardjono, P. Sinuaji, and F. Gulo, *J. Phys. Conf. Ser.* 817(1), 012052 https://doi.org/10.1088/1742-6596/817/1/012052 (2017).
17. B. Gupta, N. Kumar, K. Panda, V. Kanan, S. Joshi and I. Visoly-Fisher. *Sci. Rep*, 7(1), 1. https://doi.org/10.1038/srep45030 (2017).
18. J.B. Wu, M.L. Lin, X. Cong, H.N. Liu, and P.H. Tan, *Chem. Soc. Rev.* 47(5), 1822 https://doi.org/10.1039/C6CS00915H (2018).
19. D. Schläfer, T. Walker, N. Mattern, W. Grünberger, and D. Hinz, *TSM* 26, 71 https://doi.org/10.1155/TSM.26-27.71 (1996).
20. L.I. Yanfeng, A.H.U. Minggang, L.I. Anhua, F.E.N.G. Haibo, S. Huang, L.I. Wei, and Q. Yan, *J. Rare Earths* 32(7), 628 https://doi.org/10.1016/S1002-0721(14)60118-6 (2014).
21. E.A. Périgo, M.F. De Campos, R.N. Faria, F.J.C. Landgraf, *Powder Technol*. 224, 291. https://doi.org/10.1016/j.powtec.2012.03.010 (2012).
22. T. Minowa, M. Shimao, and M. Honshima, *J. Magn. Magn. Mater.* 97(1–3), 107 https://doi.org/10.1016/0304-8853(91)90167-9 (1991).
23. S. Dutta, S. Chattopadhyay, A. Sarkar, M. Chakrabarti, D. Sanyal, and D. Jana, *Prog. Mater. Sci.* 54(1), 89 https://doi.org/10.1016/j.pmatsci.2008.07.002 (2019).
24. Y. Qiu, F. Guo, R. Hurt, and I. Külaots, *Carbon* 72, 215 https://doi.org/10.1016/j.carbon.2014.02.005 (2014).
25. R.G.T. Fim, M.R.M. Silva, S.C. Silva, J.S.F. Casini, P.A.P. Wendhausen, and H. Takiishi, *Mater. Sci. Forum* 930, 445 https://doi.org/10.4028/www.scientific.net/MSF.930.445 (2018).
26. J. Li, H. Sepehri-Amin, T. Sasaki, T. Ohkubo, and K. Hono, *Sci. Technol. Adv. Mater.* 22(1), 386 https://doi.org/10.1080/14686996.2021.1916377 (2021).
27. P. Nothnagel, K.H. Müller, D. Eckert, and A. Handstein, *J. Magn. Magn. Mater.* 101(1–3), 379 https://doi.org/10.1016/0304-8853(91)90786-A (1991).

Springer Nature or its licensor (e.g. a society or other partner) holds exclusive rights to this article under a publishing agreement with the author(s) or other rightsholder(s); author self-archiving of the accepted manuscript version of this article is solely governed by the terms of such publishing agreement and applicable law.